Emergent quasiperiodic order in Bose-Bose mixtures induced by spin-dependent periodic potentials

Abid Ali [1,2] Pei Zhang,[2] Hiroki Saito [3] and Yong-Chang Zhang [2,*]

[1] *First Affiliated Hospital of Xi'an Jiaotong University, Xi'an 710049, People's Republic of China*

[2] *MOE Key Laboratory for Nonequilibrium Synthesis and Modulation of Condensed Matter, and Shaanxi Key Laboratory of Quantum Information and Quantum Optoelectronic Devices, School of Physics, Xi'an Jiaotong University, Xi'an 710049, People's Republic of China*

[3] *Department of Engineering Science, University of Electro-Communications, Tokyo 182-8585, Japan*

(Received 15 February 2026; accepted 16 June 2026; published 6 July 2026)

We study the ground-state and low-lying metastable phases of repulsive binary Bose-Einstein condensates confined in twisted, spin-dependent periodic optical lattices. For balanced mixtures, weak intercomponent interactions yield a fourfold momentum-space symmetry dictated by the lattice geometry. Increasing the coupling strength leads to the emergence of additional momentum peaks that combine with the lattice-induced structure to produce an eightfold rotationally symmetric pattern, signaling quasiperiodic order. At intermediate interactions, global phase separation suppresses this quasicrystalline state; however, at stronger coupling, local phase separation gives rise to a long-lived metastable phase in which the eightfold symmetry is restored. In this regime, a secondary ring of dominant momentum peaks appears at smaller wave vectors, indicating longer-wavelength density modulations and a crossover from lattice-dominated to interaction-driven quasicrystalline order. In contrast, imbalanced mixtures form partially miscible density clusters with eightfold-symmetric quasiperiodic patterns only at intermediate coupling, while stronger interactions drive global phase separation and permanently destroy quasicrystalline order. Real-time simulations demonstrate that these quasiperiodic structures are dynamically stable and experimentally accessible. Our results show that quasicrystalline order can emerge in binary condensates without explicitly quasiperiodic lattices and reveal population balance as a key ingredient for stabilizing quantum quasicrystals.

DOI: 10.1103/zt4j-57hp

I. INTRODUCTION

Quasicrystals (QCs) exhibit long-range order without translational periodicity while supporting rotational symmetries forbidden in periodic crystals, such as fivefold, eightfold, and higher-order symmetries [1–3]. Since their discovery, they have challenged the conventional framework of crystallography and provided a setting for studying nonperiodic order. Originally observed in solid-state systems, QCs have since been investigated in a wide range of contexts, including exotic quantum states of matter [4–9] and engineered systems such as photonic and topological structures [10–19], as well as quantum transport [20,21] and quantum computation [22]. Despite this progress, a central question is whether QCs can emerge as thermodynamic ground states or whether their stability requires entropy or external constraints. Addressing this question requires controllable platforms in which interactions and external potentials can be tuned independently.

Ultracold atomic gases provide a versatile platform for simulating many-body physics in a highly controllable manner, where optical lattices enable the engineering of effective lattice Hamiltonians [23]. This high degree of control has enabled the exploration of a wide range of ordered quantum phases, including proposed realizations of quasicrystalline structures in cold-atom systems [24–28]. In this context, realizations of quasicrystalline order in cold-atom systems can be broadly classified into two approaches. The first is direct imprinting, where quasiperiodic order is externally imposed through optical potentials with engineered symmetries. This approach has been demonstrated experimentally using multibeam interference patterns that generate eightfold-symmetric optical lattices; Bose-Einstein condensates (BECs) are then loaded into such lattices [29,30]. In these systems, however, quasicrystalline order is externally enforced rather than arising spontaneously from the intrinsic dynamics of the system.

Beyond externally imposed quasiperiodic structures, a second route addresses the spontaneous emergence of quasicrystalline order driven by intrinsic interactions. In this direction, several theoretical mechanisms have been proposed, including dipolar Bose gases with spin-orbit coupling, where competing interaction-induced length scales stabilize multiple quasicrystalline ground states [31]; systems with soft-core or Lifshitz-Petrich-type interactions supporting cluster quasicrystals with finite superfluidity [32]; Raman-assisted lattice schemes generating effective higher-dimensional quasicrystalline order [33]; and cavity-mediated long-range interactions leading to self-organized quasicrystalline phases [34]. Recently, the effects of quasicrystalline confinement in dipolar Bose gases have been studied in Ref. [35], where a variety of modulated and super quasicrystalline phases were reported. Despite these developments, most proposals rely on engineered interactions, external driving, or cavity-induced

*Contact author: zhangyc@xjtu.edu.cn

feedback. A minimal and experimentally accessible route to spontaneous quasicrystalline order in quantum gases therefore remains an open problem.

In this work, we propose and analyze a mechanism for emergent quasicrystalline order in a binary BEC subjected to two-dimensional spin-dependent periodic potentials. Such lattices can be realized experimentally using optical fields with controlled wave numbers and polarizations [36–43]. Unlike previous approaches, no quasiperiodic structure is imposed externally. Instead, each component experiences a distinct periodic lattice, leading to competing lattice-induced density modulations and intercomponent interactions that introduce multiple characteristic length scales. This competition drives the system across regimes of phase mixing and separation and, under appropriate conditions, results in the formation of quasicrystalline order.

Our approach differs from direct-imprinting schemes, where quasiperiodic structure is imposed by external potentials. Instead, quasicrystalline like order emerges from the interplay between intercomponent interactions and component-dependent periodic lattices. This mechanism is conceptually related to QCs formation in soft-matter systems, where competing length scales play a central role [44–50]. We study a binary BEC in the superfluid regime. Our results provide a route toward interaction-driven QCs in ultracold atomic gases and establish a feasible framework for exploring their ground-state properties.

By analyzing the ground-state behavior of this binary BEC system, we find that atom-atom contact interactions can lead to remarkable quasicrystalline density profiles within the periodic background potentials. For imbalanced mixtures, we show that the two components are partially overlapped even though $g_{12} > g$; this occurs due to density modulation within each component, which alters the global mixing energy. This partially miscible phase self-organizes into quasiperiodic modulated density clusters exhibiting eightfold rotational symmetry. In the case of a balanced mixture (i.e., when the two components have the same particle number), aperiodic density modulations emerge, accompanied by an immiscible-miscible phase transition.

The rest of this paper is organized as follows. In Sec. II, we describe the system using coupled Gross-Pitaevskii equations with a spin-dependent periodic potential. In Sec. III, we present numerical results for both balanced and imbalanced mixtures, focusing on the ground-state density profile. In Sec. IV, we exhibit real-time dynamics of the binary system. Finally, Sec. V summarizes the key findings.

II. THEORETICAL MODEL OF THE BINARY BECS

The model considered here describes a quasi-two-dimensional binary BEC [51] in the mean-field regime with tight confinement along the axial direction ($\mu \ll \hbar\omega_z$), subjected to spin-dependent two-dimensional periodic potentials. Within the mean-field approximation, the system is characterized by the macroscopic wave functions Ψ_1 and Ψ_2, whose dynamics are governed by the coupled Gross-Pitaevskii (GP) equations

$$i\hbar\frac{\partial\Psi_1}{\partial t} = \left(-\frac{\hbar^2\nabla^2}{2m_1} + V_1 + V_{\text{trap}} + g_{11}|\Psi_1|^2 + g_{12}|\Psi_2|^2\right)\Psi_1, \tag{1a}$$

$$i\hbar\frac{\partial\Psi_2}{\partial t} = \left(-\frac{\hbar^2\nabla^2}{2m_2} + V_2 + V_{\text{trap}} + g_{22}|\Psi_2|^2 + g_{21}|\Psi_1|^2\right)\Psi_2. \tag{1b}$$

For simplicity, we set $m_1 = m_2 = 1$ and $\hbar = 1$, with m_1 and m_2 denoting the atomic masses of components 1 and 2, respectively. The wave functions are normalized such that $\int d\mathbf{r}\,|\Psi_j(\mathbf{r},t)|^2 = N_j$, where N_j is the number of atoms in component $j = 1, 2$. The interaction coefficients are obtained from the three-dimensional scattering lengths $a_{jj'}$ by projecting onto the ground state of the tightly confined direction, yielding

$$g_{jj'} = \frac{g_{jj'}^{3D}}{\sqrt{2\pi}\,l_z} = \frac{4\pi\hbar^2 a_{jj'}}{m\sqrt{2\pi}\,l_z}, \tag{2}$$

where $l_z = \sqrt{\hbar/(m\omega_z)}$ is the harmonic oscillator length [51].

The external potential acting on the condensates consists of a spin-dependent periodic lattice and a circular confinement trap. The periodic potentials are given by

$$V_1(x,y) = U_1(\cos^2(kx) + \cos^2(ky)), \tag{3a}$$

$$V_2(x',y') = U_2(\cos^2(kx') + \cos^2(ky')), \tag{3b}$$

where (x', y') denotes a coordinate system rotated by an angle θ relative to (x, y):

$$\begin{pmatrix} x' \\ y' \end{pmatrix} = \begin{pmatrix} \cos\theta & -\sin\theta \\ \sin\theta & \cos\theta \end{pmatrix}\begin{pmatrix} x \\ y \end{pmatrix}. \tag{4}$$

Here $U_1 = -U_2 \equiv U$ defines the lattice depth for the two components.

To confine the condensates within a finite region, we introduce a soft circular trap,

$$V_{\text{trap}}(r) = \frac{V_0}{2}\left(1 + \tanh\frac{r - R_t}{w_t}\right), \tag{5}$$

where $r = \sqrt{x^2 + y^2}$, V_0 is the trap amplitude, R_t is the trap radius, and w_t characterizes the smoothness of the trap edge. The circular trap serves two important purposes in the context of the twisted bilayer potential: (i) It confines the condensate within the finite numerical domain, preventing the wave function from interacting with the simulation boundaries and thereby avoiding edge effects, and (ii) it preserves the rotational symmetry of the system, ensuring that the rotated lattice does not induce distortions in the density peaks in momentum space due to asymmetric boundary interactions. This form provides a nearly flat potential in the central region with smoothly varying edges, allowing the atomic density to remain uniform at the center while minimizing reflections and other numerical artifacts at the boundaries.

The two components correspond to different hyperfine states of the same atomic species (e.g., $|F = 1, m_F = 1\rangle$

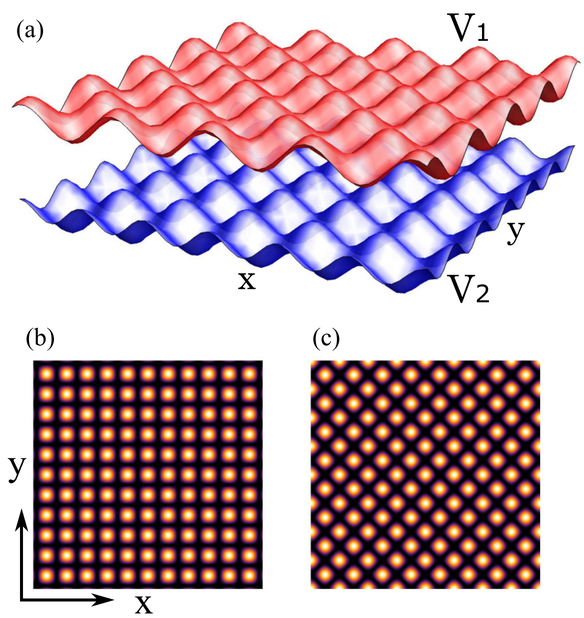

FIG. 1. (a) Schematic illustration of two independent periodic optical lattice potentials, V_1 for component 1 and V_2 for component 2. Panels (b) and (c) show the corresponding spatial profiles of V_1 and V_2 along the x and y directions, highlighting the relative orientation of the square lattices. This configuration enables independent manipulation of atoms in different spin components via spin-dependent optical lattices.

and $|F=2, m_F=0\rangle$ in ^{87}Rb), where F and m_F are the angular momentum and projection quantum numbers in the ^{87}Rb ground-state manifold. The spin-dependent periodic potentials $V_1(x, y)$ and $V_2(x', y')$ for component 1 and 2, respectively, with a fixed rotation angle $\theta = \pi/4$, are applied as shown in Fig. 1(a). These potentials are state selective via the ac Stark shift at tune-out wavelengths: Atoms in state $|1\rangle$ experience only $V_1(x, y)$, while atoms in state $|2\rangle$ experience only $V_2(x', y')$. This has been demonstrated experimentally in bilayer optical lattices [43]. This configuration creates a moiré pattern analogous to twisted bilayer systems, but here the two layers correspond to different hyperfine states of the same atomic gas rather than physically separated 2D materials.

It is worth highlighting that this twisted bilayer square lattice setting differs from the eightfold rotationally symmetric optical potentials used in Refs. [26,29,35], even though the latter are similarly generated by the superposition of two square lattices with a relative rotational angle of $\pi/4$. In the configurations considered in Refs. [26,29,35], a single-component BEC is subjected to overall quasiperiodic confinements with eightfold rotational symmetry. However, the two-layer potentials $V_{1,2}$ discussed in this work are spin-dependent and applied to different hyperfine states of the same atomic species, with each state experiencing only one periodic square optical lattice. In the following, we will demonstrate that the interplay between these periodic external confinements and the atom-atom contact interactions can lead to symmetry breaking, resulting in emergent quasiperiodic order in the BEC density profiles. This behavior contrasts sharply with the quasicrystallization predicted and observed in Refs. [26,28,29,35], which is solely induced by the external quasiperiodic potentials.

III. GROUND-STATE PROPERTIES

We consider a two-dimensional binary BEC subjected to spin-dependent periodic potentials and a soft circular trapping potential, as described in Eq. (5). The imaginary-time propagation of Eq. (1) is employed to determine the ground state, where the imaginary unit i is replaced with -1 using a pseudospectral method [52]. Numerically, the system is discretized on a uniform Cartesian grid with spatial resolution $dx = dy = 2\pi/64$ and a time step $dt = 0.001$. The circular trap ensures smooth confinement within the simulation box, minimizing boundary artifacts while maintaining a nearly uniform density in the central region. We add a small random number of amplitude 10^{-3} to each mesh point of the initial state at $t = 0$ to break symmetry.

Throughout the simulations, we use dimensionless quantities. We normalize length, energy, and wave functions as $\tilde{\mathbf{r}} = k\mathbf{r}$, $\tilde{E} = mE/(\hbar^2k^2)$, and $\tilde{\Psi}_j = \Psi_j/\sqrt{n_0}$, where π/k is the spacing of the periodic potential and $n_0 = N/A$ is the average areal density. Here $N = N_1 + N_2$ is the total number of atoms and A is the area of the two-dimensional system. The dimensionless trapping potential and interaction coefficients are $\tilde{V}_{\rm trap} = mV_{\rm trap}/(\hbar^2k^2)$, $\tilde{V}_j = mV_j/(\hbar^2k^2)$, and $\tilde{g}_{jj'} = mn_0g_{jj'}/(\hbar^2k^2)$. We assume equal intracomponent interactions, $g_{11} = g_{22} \equiv g = 15$. In the following, the tildes are omitted for simplicity.

After setting up the system as described, we first examine the case of a balanced mixture, where the populations of components 1 and 2 are equal. Figure 2 shows the corresponding ground-state density profiles $|\Psi_1|^2$ and $|\Psi_2|^2$, which exhibit QCs density patterns arising from the combined effects of the intercomponent interaction g_{12} and the spin-dependent periodic optical lattice potentials V_1 and V_2. The external potentials act independently on each component, while the interaction strength g_{12} determines the degree of spatial overlap between them.

In Fig. 2(a), the real-space density distributions follow the underlying square-lattice geometry, with component 2 rotated according to the potential $V_2(x', y')$. As the intercomponent interaction g_{12} increases, the coupling between the two layers strengthens and progressively distorts the original lattice order. For sufficiently strong coupling (e.g., $g_{12} = 10.5$), the periodic density modulations are replaced by quasiperiodic patterns in both components, as illustrated in Fig. 2(c). The middle panels of Fig. 2 show the density profiles along $y = 0$, where both components exhibit quasiperiodic modulations that become increasingly pronounced with growing g_{12}.

At weak coupling ($g_{12} = 1.5$), the momentum-space distributions exhibit four low-intensity peaks per component, consistent with the $\pi/4$ rotation between the two square lattices. These lattice-related peaks set the dominant modulation length scale imposed by the optical potentials. As g_{12} increases, the four primary peaks become more pronounced, and at $g_{12} = 10.5$ [Fig. 2(c)] weak secondary peaks appear, diagonally in component 1 and off-diagonally in component 2; these secondary peaks signal the onset of quasicrystalline correlations, although their intensity is still small. With a

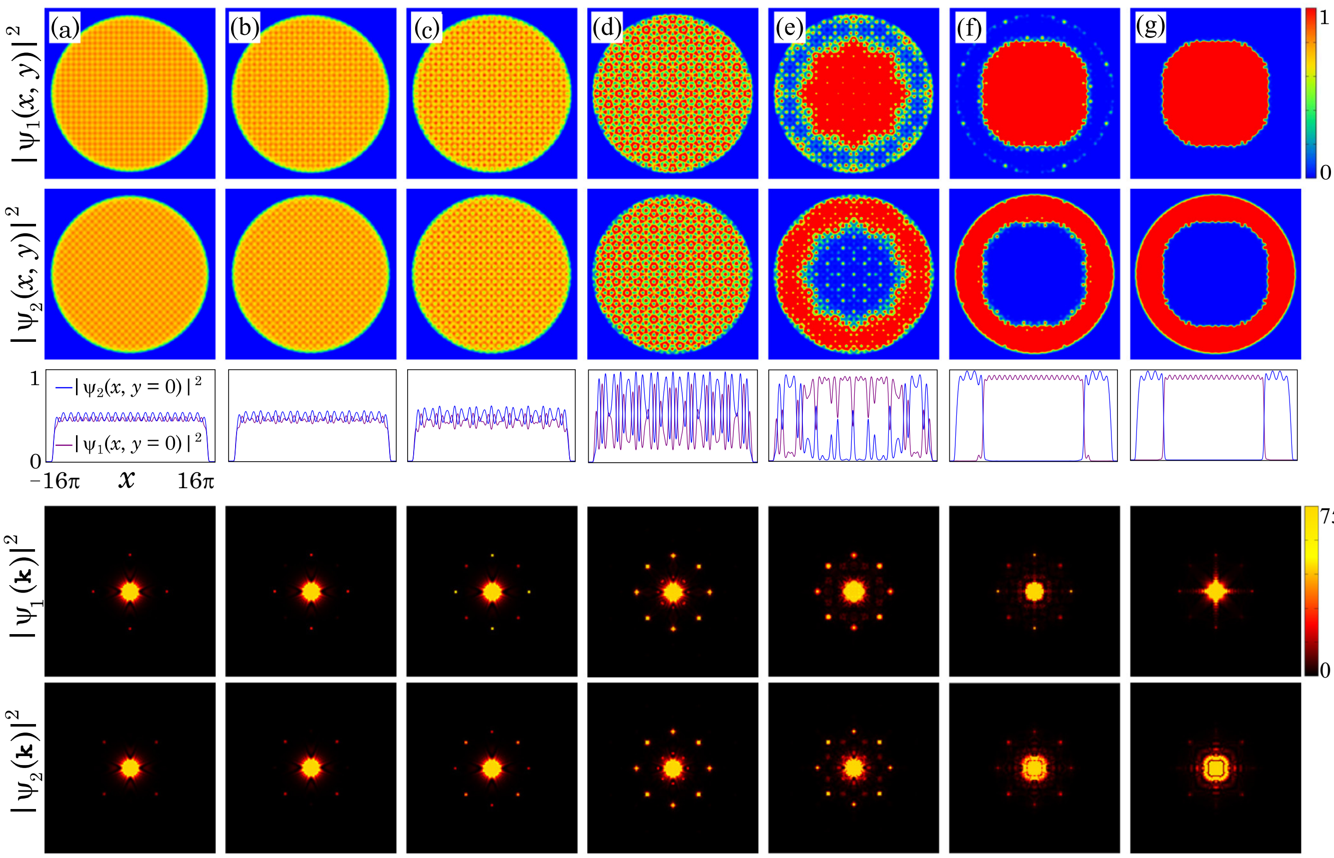

FIG. 2. Ground-state density distributions of components 1 and 2 in a balanced binary BEC. The intracomponent interactions are fixed at $g_{11} = g_{22} \equiv g = 15$, with lattice depth $U = 1.2$. The circular box trap parameters are $V_0 = 50$, $R_t = 15\pi$, and $w_t = 2$. The middle panels show line profiles along $y = 0$, $|\Psi_j(x, y = 0)|^2$, while the bottom panels display the corresponding momentum-space distributions. Panels (a)–(f) correspond to intercomponent interaction strengths $g_{12} = 1.5$, 6, 10.5, 15.15, 15.25, 15.35, and 15.65, respectively. Each real-space panel spans a spatial domain of $(32\pi)^2$, and each momentum-space panel spans $(3\pi)^2$.

further increase to $g_{12} = 15.15$ [Fig. 2(d)], the secondary peaks strengthen and, together with the four lattice-induced peaks, produce eight distinct peaks that define a clear eightfold rotational symmetry.

With further increasing intercomponent interaction strength, the balance between mixing and segregation changes qualitatively. At $g_{12} = 15.25$ [Fig. 2(e)], the two condensates start to separate into extended domains; nevertheless, the momentum distributions of both components still display a clear eightfold rotational symmetry. Upon slightly increasing the coupling to $g_{12} = 15.35$ [Fig. 2(f)], global phase separation becomes dominant, accompanied by a noticeable reduction in the intensity of the secondary momentum peaks. At even stronger coupling, $g_{12} = 15.65$ [Fig. 2(g)], the system forms fully separated macroscopic domains, and the secondary peaks vanish entirely, leaving no signature of quasicrystalline order in the ground state. This evolution from fourfold lattice-induced symmetry at weak coupling to eightfold rotational symmetry at intermediate coupling provides direct evidence of quasicrystalline order in a binary BEC realized here without the need for an externally imposed quasiperiodic lattice [26,29,35].

Thus, the quasicrystalline order occupies a stable window $\Delta g_{12} \approx 4.75$, from $g_{12} \approx 10.5$ to the onset of global phase separation at $g_{12} \approx 15.25$. The observed patterns arise from a superposition of the two spin-dependent periodic potentials mediated by g_{12}, which drives quasicrystalline order. To understand the phase separation threshold, we recall the standard miscibility condition for a homogeneous binary BEC without external potentials: $g_{11}g_{22} - g_{12}^2 > 0$ for miscibility, and $g_{11}g_{22} - g_{12}^2 < 0$ for phase separation. With $g_{11} = g_{22} = g = 15$, this predicts a threshold at $g_{12} = g = 15$. In our system, however, the spin-dependent lattice potentials break translational symmetry and induce density modulations, shifting the effective threshold to $g_{12} \approx 15.25$. This lattice-induced shift arises because the spin-dependent periodic potentials modulate the local density in each component, thereby modifying the global mixing energy.

In contrast, Fig. 3 presents the energies of the ground and metastable states as a function of the intercomponent interaction strength g_{12}. Figures 3(a) and 3(b) correspond to the ground state, whereas Figs. 3(c)–3(f) show distinct metastable configurations that evolve differently as g_{12} is increased. These metastable states are characterized by locally phase-separated regions with alternating, finely modulated density patterns.

Notably, the momentum-space distributions corresponding to the real-space configurations in Figs. 3(b) and 3(c) exhibit an abrupt disappearance of eightfold symmetry as a consequence of global phase separation. In contrast, for the

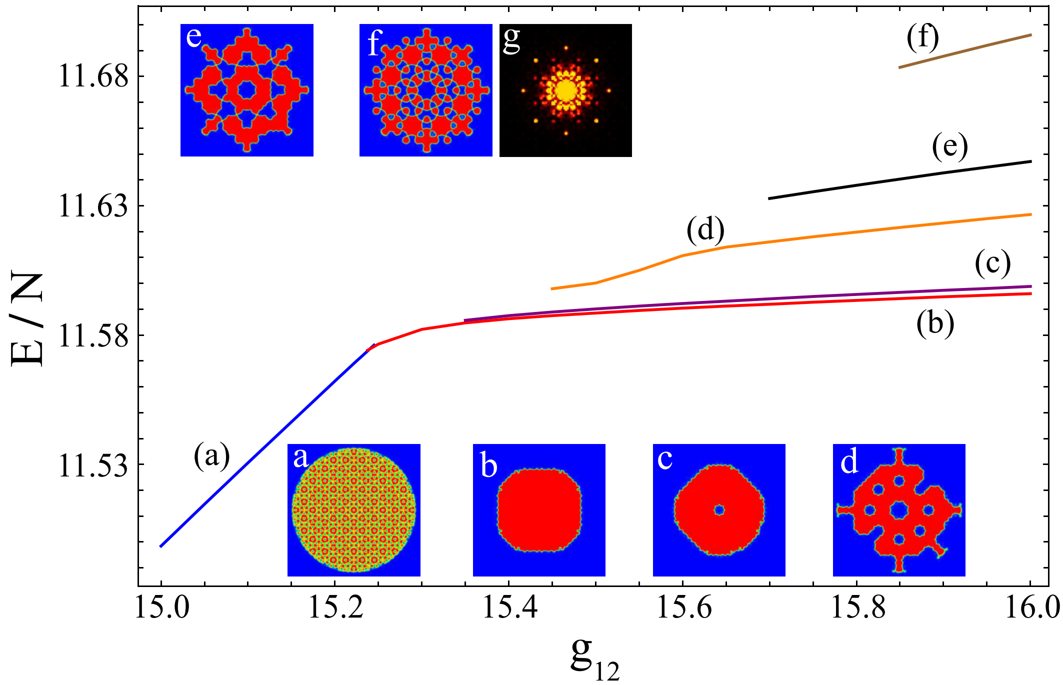

FIG. 3. Energies of the ground and metastable states as a function of the intercomponent interaction strength g_{12} for the balanced mixture. Solid lines indicate the energies of the respective states. Insets show the real-space density distribution of component 1 for each case. Other parameters are the same as in Fig. 2. Real-space densities are plotted over a spatial domain of $(32\pi)^2$, and the corresponding momentum-space distribution for the case shown in panel (f) is displayed in panel (g), spanning $(2\pi)^2$.

locally phase-separated configurations shown in Figs. 3(d)–3(f), the alternating, finely modulated density regions lead to a reemergence of eightfold symmetry in momentum space, accompanied by sharper and more intense secondary peaks. Figure 3(g) displays the momentum-space distribution corresponding to the real-space density in Fig. 3(f), demonstrating that quasicrystalline order can persist robustly in metastable states. Nevertheless, these configurations do not correspond to the true ground state of the system.

The reemergence of eightfold symmetry in the metastable configuration [Fig. 3(f)] is driven by a change in the characteristic length scale of density modulation. For weak and intermediate interactions, momentum peaks are determined primarily by the underlying lattice vectors, reflecting lattice-dominated quasicrystallinity. At stronger coupling (e.g., $g_{12} = 16$), a second ring of eight dominant peaks emerges at smaller momenta, while the original outer ring remains visible. These inner peaks correspond to longer-wavelength real-space modulations induced by local phase separation. The coexistence of the two momentum-space rings thus signals a crossover from a lattice-controlled to an interaction-dominated quasicrystalline regime.

Next we consider a density-imbalanced mixture at fixed total average density, where component 1 contributes a fraction 0.1 of the total density and component 2 the remaining fraction 0.9. Focusing on the repulsive regime with $g_{12} > g$, Figs. 4(a) and 4(b) show that for $g_{12} = 15.15$ and 15.3 (with $g = 15$), the two components coexist and form partially miscible density clusters arranged in an quasiperiodic pattern exhibiting clear eightfold rotational symmetry.

The density profile along $y = 0$, corresponding to Fig. 4(a), clearly reveals quasiperiodic density modulations similar to those observed in experiments employing eightfold quasiperiodic optical lattices [30]. Increasing the intercomponent repulsion to $g_{12} = 15.9$ drives a transition from the partially miscible eightfold quasicrystalline state to a fully phase-separated configuration, as shown in Fig. 4(c). In this regime, the minority component is expelled from the central region and accumulates near the edges of the circular trap, while the majority component occupies the inner region and develops a periodic modulation [the density profile along $y = 0$ in the bottom panel of Fig. 4(c)]. This spatial segregation marks the breakdown of the partially miscible quasicrystalline order, with the eightfold rotational symmetry abruptly disappearing in momentum space, as evident in Fig. 4(f).

A characteristic feature of the imbalanced regime is seen in the minority component, shown in Fig. 4(e), which exhibits pronounced low-momentum peaks. In contrast, the majority component shows only weak Fourier signatures of the eightfold quasicrystalline structure. This behavior arises from the combined effect of the spin-dependent optical lattice ($U = 1.2$) and the intercomponent interaction g_{12} in the presence of a 45° twist between the lattice geometries, which together determine the effective quasicrystalline structure.

Due to the strong density imbalance, the majority component (carrying 90% of the total density) responds only weakly to this combined lattice–interaction-induced structure. Within the GP framework, interaction-induced smoothing further suppresses higher-order Fourier components, leaving only low-contrast eightfold signatures in its momentum distribution, located near ±2 [lower panel of Fig. 4(e)].

Through the intercomponent mean-field coupling $g_{12}|\Psi_2|^2\Psi_1$, this weak spatial modulation of the majority component acts as an effective potential for the minority

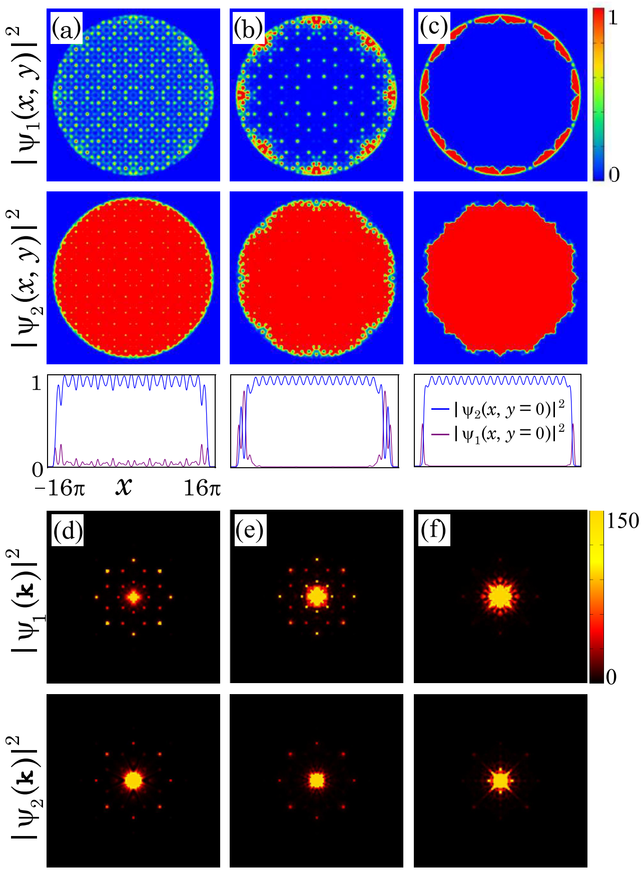

FIG. 4. Ground-state density distributions of an imbalanced binary BEC in a spin-dependent periodic lattice. Panels (a)–(c) show the system for increasing intercomponent interactions $g_{12} = 15.15$, 15.3, and 15.9, respectively. The bottom panels display line profiles along $y = 0$, $|\Psi_j(x, y = 0)|^2$, and the corresponding momentum-space distributions. For moderate g_{12} in panels (a) and (b), the condensates form partially miscible quasicrystalline density clusters with eightfold rotational symmetry, whereas for stronger g_{12} in panel (c), the components undergo global phase separation and the quasicrystalline signature disappears. Other parameters are the same as in Fig. 2. Each real-space panel spans a spatial domain of $(32\pi)^2$, and each momentum-space panel spans $(3\pi)^2$.

component. In this regime, the back-action of the minority component on the majority is negligible to leading order, so the minority component evolves in an effectively static background set by the majority density. This leads to enhanced imprinting of the spatial modulation and a corresponding redistribution of spectral weight in momentum space.

This behavior is consistent with the real-space density of the minority component in Fig. 4(b), where an eightfold modulation develops over a characteristic length scale. In Fourier space, a central single blob appears at $k \approx 0$, reflecting the condensate fraction, together with eight finite-k peaks. These consist of axial peaks at $(\pm 0.81, 0)$ and $(0, \pm 0.81)$ and diagonal peaks at $(\pm 0.56, \pm 0.56)$, as shown in Fig. 4(e). The dominant axial peaks at $k \approx 0.81$ set the primary real-space modulation scale, corresponding to a wavelength $\lambda \sim 8$, consistent with the spacing observed in Fig. 4(b). Additional peaks at $(\pm 2, 0)$ and $(0, \pm 2)$ reflect the underlying twisted lattice geometry and associated eightfold correlations. In the balanced case, by contrast, comparable densities in both components produce strong mutual back-action and self-consistent mean-field dressing, which redistributes spectral weight more symmetrically and yields quasicrystalline peaks of nearly equal intensity, as shown in Fig. 2(d).

Comparing balanced and imbalanced mixtures highlights a fundamental difference in how the two systems respond to increasing intercomponent interactions. In both cases, sufficiently strong coupling initially drives the system into a globally phase-separated state, accompanied by the disappearance of quasicrystalline order, as shown for the balanced mixture in Fig. 2(g) and for the imbalanced mixture in Fig. 4(c).

Upon increasing the intercomponent interaction, the system develops qualitatively different stationary solutions within the mean-field framework. All results are obtained by solving Eq. (1) using imaginary-time propagation. Starting from different initial conditions allows convergence to distinct local minima of the energy functional, where the lowest-energy solution is identified as the ground-state and higher-energy solutions are classified as metastable states. To construct Fig. 3, each stationary solution is then continued as a function of the intercomponent interaction strength g_{12}, and its energy per particle is evaluated. The resulting curves represent branches of stationary mean-field solutions (ground and metastable) rather than a thermodynamic phase diagram or a dynamical parameter ramp.

In the balanced mixture, an unexpected re-emergence of quasicrystalline order is found along one of these metastable branches. The corresponding density profiles reorganize into a locally phase-separated configuration [Fig. 3(f)], while the momentum distribution [Fig. 3(g)] recovers a pronounced eightfold rotational symmetry. This state lies at higher energy than the corresponding ground-state solution at the same intercomponent interaction strength g_{12}.

In sharp contrast, the imbalanced mixture shows no such recovery. Even at larger values of g_{12}, the system remains globally phase separated, and the quasicrystalline peaks do not reappear in momentum space. The minority component is too dilute to form the alternating local domains required to reconstruct eightfold ordering. These results demonstrate that population balance plays a crucial role. In balanced binary condensates, reentrant quasicrystalline order appears in metastable stationary solutions of Eq. (1) (Fig. 3), but such order is absent in the corresponding ground state (Fig. 2). By contrast, in imbalanced systems, global phase separation sets in, and quasicrystalline signatures vanish upon increasing the intercomponent interaction strength g_{12} (Fig. 4).

To quantify the spatial overlap between the two condensates in the balanced and imbalanced case, we define the normalized overlap parameter

$$\mathcal{O} = \frac{\int d\mathbf{r}\, |\Psi_1(\mathbf{r})|^2\, |\Psi_2(\mathbf{r})|^2}{\sqrt{\left(\int d\mathbf{r}\, |\Psi_1(\mathbf{r})|^4\right)\left(\int d\mathbf{r}\, |\Psi_2(\mathbf{r})|^4\right)}}. \tag{6}$$

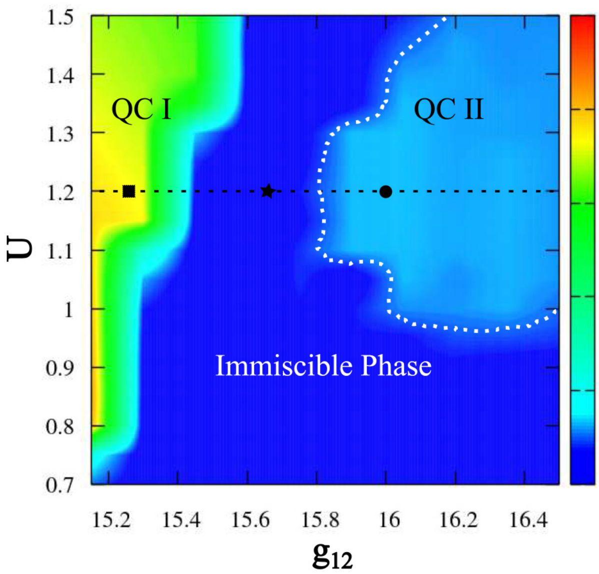

FIG. 5. Phase diagram of the balanced binary BEC in the (g_{12}, U) plane, obtained from the overlap parameter $\mathcal{O}$ defined in Eq. (6). The black square marks the parameters of Fig. 2(e), corresponding to a quasicrystalline phase (QC I) where the system begins to segregate into large spatial domains while retaining eightfold symmetry in momentum space. The black star indicates the globally immiscible phase shown in Fig. 2(f), where $\mathcal{O} = 0$ and quasicrystalline order is lost. The black circle denotes the metastable quasicrystalline regime (QC II) of Fig. 3(f), where density modulations reemerge and the momentum distribution recovers eightfold rotational symmetry despite local phase separation.

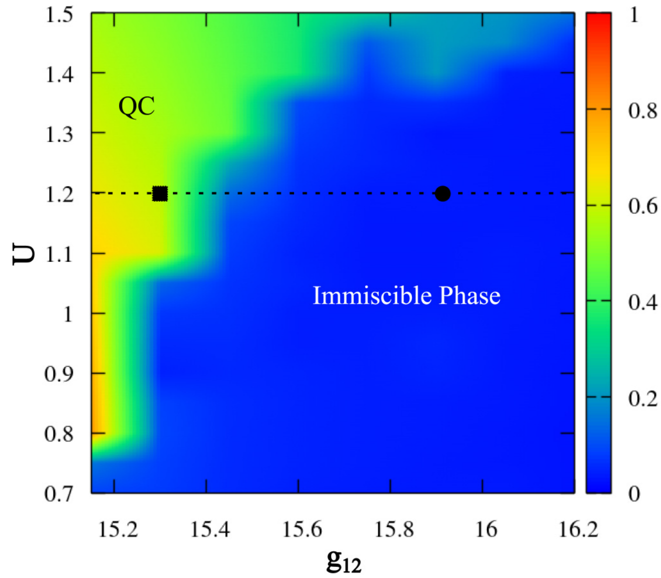

FIG. 6. Phase diagram of the imbalanced binary BEC in the (g_{12}, U) plane, obtained from the overlap parameter $\mathcal{O}$. The black square marks the coexistence phase exhibiting quasicrystalline order [Fig. 4(b)], while the black circle indicates the fully immiscible phase [Fig. 4(c)].

By definition, $\mathcal{O} = 0$ corresponds to completely separated components, while larger values indicate stronger spatial mixing.

Figures 5 and 6 show the phase diagrams obtained by evaluating $\mathcal{O}$ as a function of the lattice depth U and the intercomponent interaction strength g_{12}.

In the balanced mixture (Fig. 5), the black square marks the parameters used in Fig. 2(e), corresponding to the transition from QC I to the globally phase-separated state. The black star indicates the parameters of Fig. 2(f), where the overlap vanishes ($\mathcal{O} = 0$), signaling full phase separation. The black circle denotes the parameters of Fig. 3(f), corresponding to QC II, in which density modulations reappear and the momentum distribution restores eightfold rotational symmetry despite local phase separation.

In the imbalanced mixture (Fig. 6), two distinct regimes are observed: a QC phase, in which the components remain partially miscible and occupy overlapping regions, and an immiscible phase, where the minority component is expelled toward the edges of the trap. The black square indicates the parameters of Fig. 4(b), where the density self-organizes into a quasiperiodic pattern exhibiting eightfold rotational symmetry. The black circle corresponds to Fig. 4(c), representing a fully phase-separated state in which the eightfold symmetry is lost and the momentum distribution no longer displays quasicrystalline features.

The disappearance of QC order with increasing g_{12} is a crossover. This is reflected in the smooth evolution of the overlap parameter $\mathcal{O}$ and the gradual loss of eightfold rotational symmetry in momentum space.

IV. REAL-TIME EVOLUTION OF DYNAMICS

We analyze the real-time dynamics of binary BEC in spin-dependent periodic lattices following a quench of the lattice potential. The system is initialized at $t = 0$ in a uniform state $\Psi_j = 1/\sqrt{2}$ with small random perturbations. This uniform state is the ground state for the potential strength ($U = 0$). We then abruptly turn on the spin-dependent periodic lattice potential to a strength of $U = 1.2$. In Fig. 7 (balanced mixtures with $g_{12} = 16.5$), initial fluctuations develop into four lattice-induced peaks in momentum space by $t = 0.2$, with low-intensity secondary peaks emerging diagonally in component 1 and off-diagonally in component 2. By $t = 0.5$, these secondary peaks grow in intensity and, together with the primary lattice-induced peaks, form a clear eightfold rotationally symmetric pattern, which persists at later times despite local phase separation, although the outer peaks slightly decrease in intensity. In imbalanced mixtures ($g_{12} = 15.15$, Fig. 8), the minority component develops eight prominent peaks by $t = 0.4$, while the majority shows four dominant peaks with weaker secondary peaks. By $t = 1.0$, both components exhibit eightfold symmetry and quasiperiodic density clusters, but at $t = 5.0$, the symmetry is partially distorted as minority peaks weaken and majority outer peaks reduce to four. This comparison demonstrates that quasicrystalline order is robust in balanced mixtures but more fragile in imbalanced ones, highlighting the stabilizing role of population balance.

V. CONCLUSION

We have investigated the formation of QCs ground states in two-component BEC loaded into spin-dependent periodic

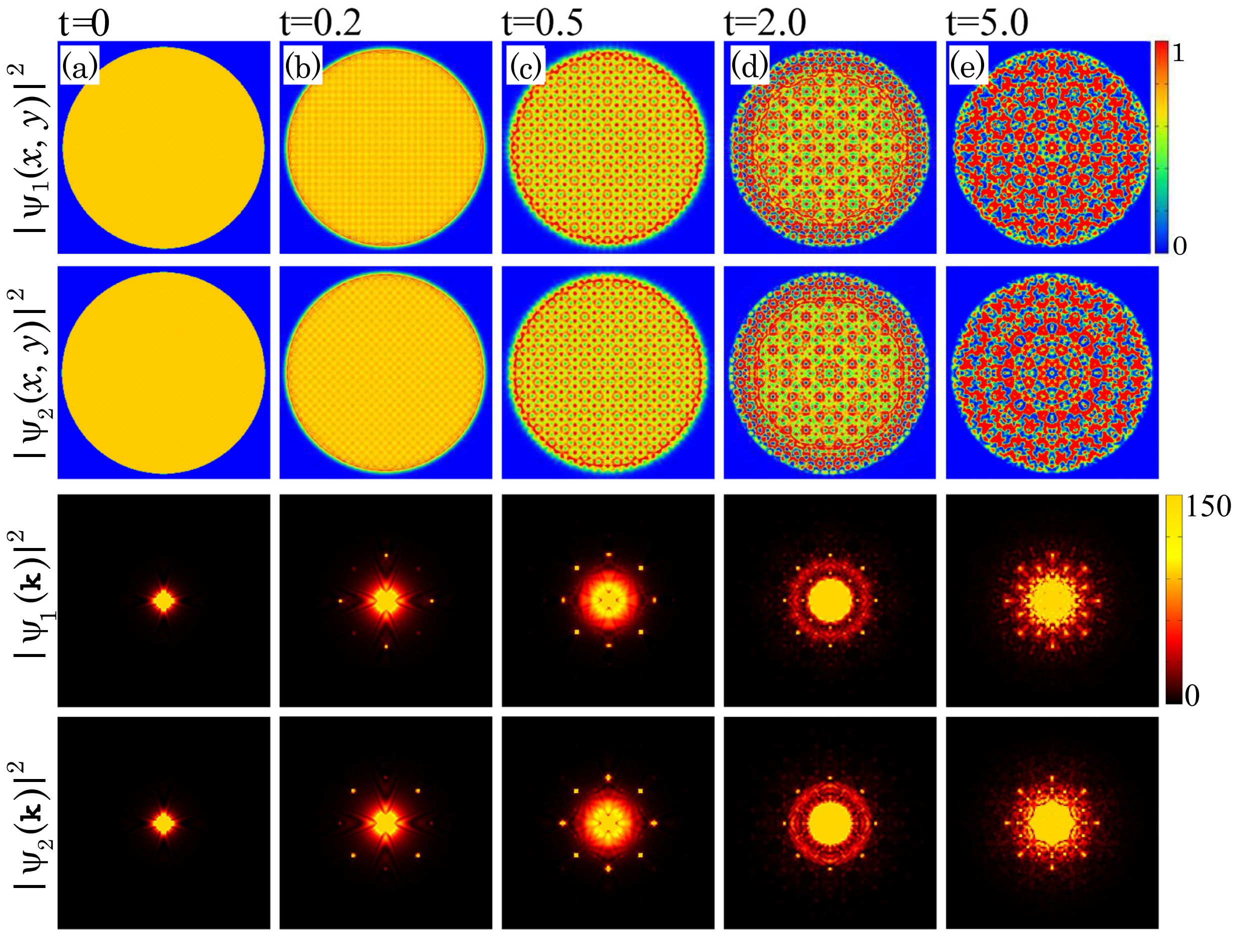

FIG. 7. Real-time evolution of a balanced binary BEC in a spin-dependent periodic lattice following a quench of the lattice potential from $U = 0$ to $U = 1.2$. The system is initialized at $t = 0$ in a uniform state $|\Psi_j| = 1/\sqrt{2}$ with small random fluctuations, corresponding to the ground state at $U = 0$. The intercomponent interaction strength is $g_{12} = 16.5$. All other parameters and the sizes of the real- and momentum-space panels are identical to those in Fig. 2.

optical lattices. The interplay between intercomponent interactions and component-dependent lattice potentials produces quasiperiodic modulated density patterns, with the miscible-immiscible transition strongly shaping the overall structure.

In balanced mixtures, weak intercomponent interactions give rise to fourfold symmetry in momentum space for each component, reflecting the underlying lattice geometry and the relative twist of $\pi/4$. As g_{12} increases, secondary peaks appear diagonally in component 1 and off-diagonally in component 2. These peaks combine with the four lattice-induced peaks to form eightfold rotational symmetry, signaling the emergence of quasicrystalline order. At stronger interactions, global phase separation suppresses this symmetry in momentum space. Upon further increasing g_{12}, local phase separation develops, the density patterns reemerge, and the eightfold symmetry is restored in a long-lived metastable state, demonstrating the robustness of quasicrystalline order in balanced mixtures.

In imbalanced mixtures, partially miscible density clusters form at intermediate g_{12}, arranging into eightfold rotationally symmetric QCs patterns. At larger intercomponent interactions, global phase separation occurs and the quasicrystalline signatures vanish permanently. Real-time simulations confirm that these quasiperiodic structures are dynamically stable and experimentally accessible.

In contrast to single-component BECs, where quasicrystalline order typically requires explicitly quasiperiodic potential with fivefold, eightfold, or higher rotational symmetry, our results demonstrate that binary condensates in spin-dependent periodic lattices can spontaneously form quasicrystalline phases without any quasiperiodic confinement. The competition between intercomponent interactions and external periodic potentials drives this emergent order, providing a highly tunable platform to explore quantum QCs and their fundamental properties, including excitation spectra [53], quantum transport [21], and potential applications in quantum simulation and computation [22].

ACKNOWLEDGMENTS

This work was supported by the National Key Research and Development Program of China (Grant No. 2021YFA1401700), Shaanxi Academy of Fundamental Sciences (Mathematics, Physics) (Grant No. 22JSY036). Y.C.Z.

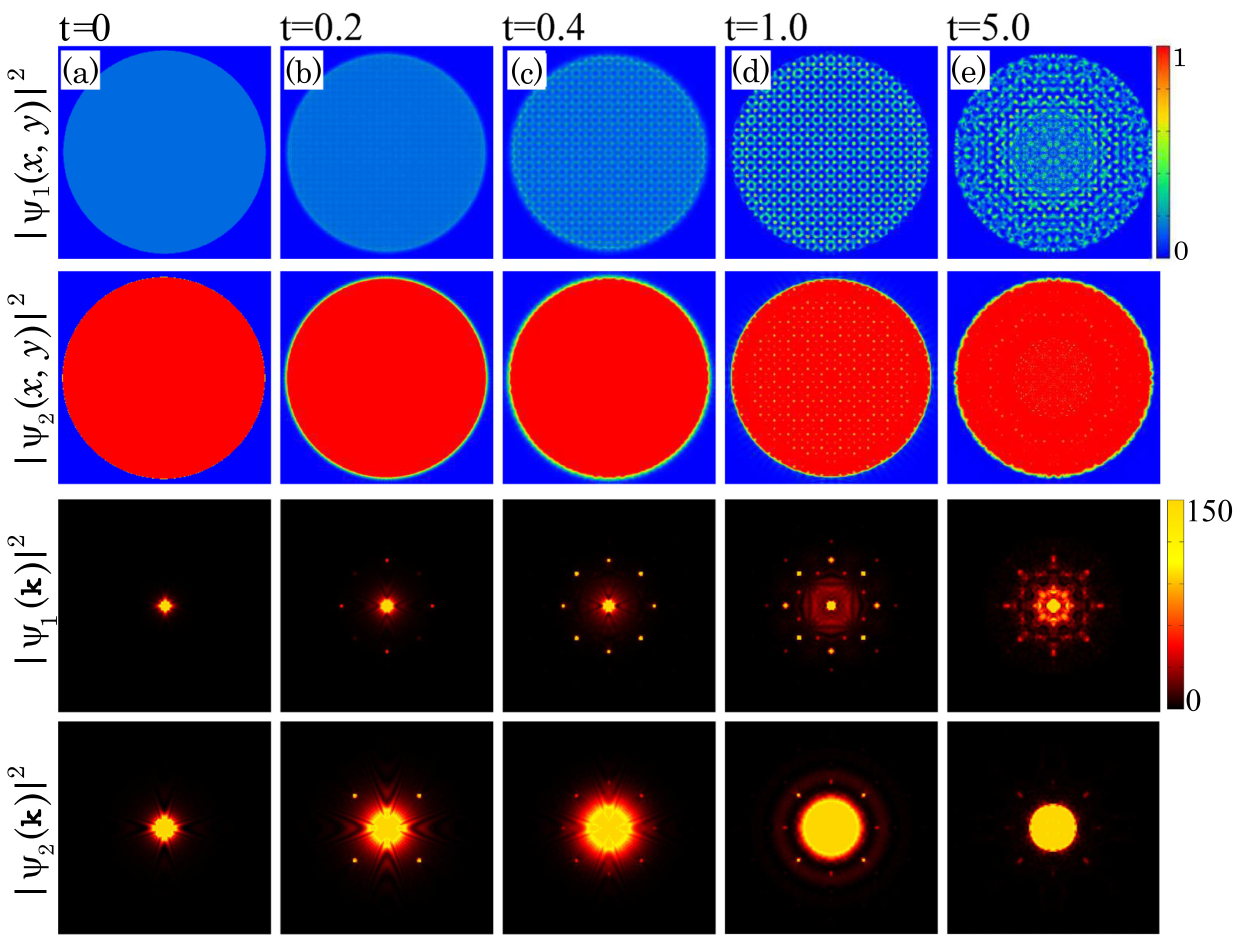

FIG. 8. Real-time evolution of a population-imbalanced binary BEC in a spin-dependent periodic lattice following a quench of the lattice amplitude from $U = 0$ to $U = 1.2$. The system is prepared with a fixed population imbalance $N_1 : N_2 = 0.1 : 0.9$, and the total mean density is normalized to unity. The intercomponent interaction strength is $g_{12} = 15.15$. All remaining parameters, as well as the spatial and momentum-space domains, are identical to those in Fig. 2.

acknowledges the support of the Xiaomi Young Talents program, Xi'an Jiaotong University through the "Young Top Talents Support Plan" and Basic Research Funding, as well as the High-performance Computing Platform of Xi'an Jiaotong University for the computing facilities. H.S. acknowledges the support by JSPS KAKENHI Grant No. JP23K03276.

DATA AVAILABILITY

The data that support the findings of this article are not publicly available upon publication because it is not technically feasible and/or the cost of preparing, depositing, and hosting the data would be prohibitive within the terms of this research project. The data are available from the authors upon reasonable request.

[1] J. Christian, *Neutron and Synchrotron Radiation for Condensed Matter Studies* (Springer, Berlin, 1994).

[2] D. Levine and P. J. Steinhardt, Quasicrystals: A new class of ordered structures, Phys. Rev. Lett. **53**, 2477 (1984).

[3] W. Steurer, Quasicrystals: What do we know? What do we want to know? What can we know? Acta Cryst. A **74**, 1 (2018).

[4] D. Gomila and D. Walgraef, Minimal model dynamics for 12-fold quasipatterns, Phys. Rev. E **89**, 032923 (2014).

[5] S. J. Ahn, P. Moon, T.-H. Kim, H.-W. Kim, H.-C. Shin, E. H. Kim, H. W. Cha, S.-J. Kahng, P. Kim, M. Koshino, Y.-W. Son, C.-W. Yang, and J. R. Ahn, Dirac electrons in a dodecagonal graphene quasicrystal, Science **361**, 782 (2018).

[6] X. Deng, S. Ray, S. Sinha, G. V. Shlyapnikov, and L. Santos, One-dimensional quasicrystals with power-law hopping, Phys. Rev. Lett. **123**, 025301 (2019).

[7] V. Heinonen, K. J. Burns, and J. Dunkel, Quantum hydrodynamics for supersolid crystals and quasicrystals, Phys. Rev. A **99**, 063621 (2019).

[8] A. Mendoza-Coto, R. Turcati, V. Zampronio, R. Díaz-Méndez, T. Macrì, and F. Cinti, Exploring quantum quasicrystal patterns: A variational study, Phys. Rev. B **105**, 134521 (2022).

[9] M. Ciardi, A. Angelone, F. Mezzacapo, and F. Cinti, Quasicrystalline Bose glass in the absence of disorder and quasidisorder, Phys. Rev. Lett. **131**, 173402 (2023).

[10] D. Louzguine-Luzgin and A. Inoue, Formation and properties of quasicrystals, Annu. Rev. Mater. Res. **38**, 403 (2008).

[11] K. Edagawa, K. Suzuki, and S. Takeuchi, High resolution transmission electron microscopy observation of thermally fluctuating phasons in decagonal Al-Cu-Co, Phys. Rev. Lett. **85**, 1674 (2000).

[12] A. Simonov and A. L. Goodwin, Designing disorder into crystalline materials, Nat. Rev. Chem. **4**, 657 (2020).

[13] B. Freedman, G. Bartal, M. Segev, R. Lifshitz, D. N. Christodoulides, and J. W. Fleischer, Wave and defect dynamics in nonlinear photonic quasicrystals, Nature (London) **440**, 1166 (2006).

[14] W. Jin and Y. Gao, Optically induced two-dimensional photonic quasicrystal lattices in iron-doped lithium niobate crystal with an amplitude mask, Appl. Phys. Lett. **101**, 141104 (2012).

[15] Z. V. Vardeny, A. Nahata, and A. Agrawal, Optics of photonic quasicrystals, Nat. Photon. **7**, 177 (2013).

[16] Y. E. Kraus, Y. Lahini, Z. Ringel, M. Verbin, and O. Zilberberg, Topological states and adiabatic pumping in quasicrystals, Phys. Rev. Lett. **109**, 106402 (2012).

[17] Y. Wang, Y.-H. Lu, J. Gao, K. Sun, Z.-Q. Jiao, H. Tang, and X.-M. Jin, Quantum topological boundary states in quasi-crystals, Adv. Mater. **31**, 1905624 (2019).

[18] D. V. Else, S.-Jie Huang, A. Prem, and A. Gromov, Quantum many-body topology of quasicrystals, Phys. Rev. X **11**, 041051 (2021).

[19] S. Weidemann, M. Kremer, S. Longhi, and A. Szameit, Topological triple phase transition in non-Hermitian Floquet quasicrystals, Nature (London) **601**, 354 (2022).

[20] P. Chawla, C. V. Ambarish, and C. M. Chandrashekar, Quantum percolation in quasicrystals using continuous-time quantum walk, J. Phys. Commun. **3**, 125004 (2019).

[21] Y. Xing, L. Qi, X. Zhao, Z. Lü, S. Liu, S. Zhang, and H.-F. Wang, Quantum transport in a one-dimensional quasicrystal with mobility edges, Phys. Rev. A **105**, 032443 (2022).

[22] M. Amaral, D. Chester, F. Fang, and K. Irwin, Exploiting anyonic behavior of quasicrystals for topological quantum computing, Symmetry **14**, 1780 (2022).

[23] C. Gross and I. Bloch, Quantum simulations with ultracold atoms in optical lattices, Science **357**, 995 (2017).

[24] L. Sanchez-Palencia and L. Santos, Bose-Einstein condensates in optical quasicrystal lattices, Phys. Rev. A **72**, 053607 (2005).

[25] N. Macé, A. Jagannathan, and M. l Duneau, Quantum simulation of a 2D quasicrystal with cold atoms, Crystals **6**, 124 (2016).

[26] R. Gautier, H. Yao, and L. Sanchez-Palencia, Strongly interacting bosons in a two-dimensional quasicrystal lattice, Phys. Rev. Lett. **126**, 110401 (2021).

[27] M. Khazali, Rydberg noisy dressing and applications in making soliton molecules and droplet quasicrystals, Phys. Rev. Res. **3**, L032033 (2021).

[28] Z. Zhu, H. Yao, and L. Sanchez-Palencia, Thermodynamic phase diagram of two-dimensional bosons in a quasicrystal potential, Phys. Rev. Lett. **130**, 220402 (2023).

[29] K. Viebahn, M. Sbroscia, E. Carter, J. Yu, and U. Schneider, Matter-wave diffraction from a quasicrystalline optical lattice, Phys. Rev. Lett. **122**, 110404 (2019).

[30] M. Sbroscia, K. Viebahn, E. Carter, J. Yu, A. Gaunt, and U. Schneider, Observing localization in a 2D quasicrystalline optical lattice, Phys. Rev. Lett. **125**, 200604 (2020).

[31] S. Gopalakrishnan, I. Martin, and E. A. Demler, Quantum quasicrystals of spin-orbit-coupled dipolar bosons, Phys. Rev. Lett. **111**, 185304 (2013).

[32] G. Pupillo, P. Ziherl, and F. Cinti, Quantum cluster quasicrystals, Phys. Rev. B **101**, 134522 (2020).

[33] J. Hou, H. Hu, K. Sun, and C. Zhang, Superfluid-quasicrystal in a Bose-Einstein condensate, Phys. Rev. Lett. **120**, 060407 (2018).

[34] F. Mivehvar, H. Ritsch, and F. Piazza, Emergent quasicrystalline symmetry in light-induced quantum phase transitions, Phys. Rev. Lett. **123**, 210604 (2019).

[35] V. Zampronio, A. M. -Coto, T. Macrì, and F. Cinti, Exploring quantum phases of dipolar gases through quasicrystalline confinement, Phys. Rev. Lett. **133**, 196001 (2024).

[36] O. Mandel, M. Greiner, A. Widera, T. Rom, T. W. Hänsch, and I. Bloch, Coherent transport of neutral atoms in spin-dependent optical lattice potentials, Phys. Rev. Lett. **91**, 010407 (2003).

[37] L. J. LeBlanc and J. H. Thywissen, Species-specific optical lattices, Phys. Rev. A **75**, 053612 (2007).

[38] B. Gadway, D. Pertot, R. Reimann, and D. Schneble, Superfluidity of interacting bosonic mixtures in optical lattices, Phys. Rev. Lett. **105**, 045303 (2010).

[39] B. Arora, M. Safronova, and C. W. Clark, Tune-out wavelengths of alkali-metal atoms and their applications, Phys. Rev. A **84**, 043401 (2011).

[40] K. Wen, Z. Meng, L. Wang, L. Chen, L. Huang, P. Wang, and J. Zhang, Experimental study of tune-out wavelengths for spin-dependent optical lattice in ^{87}Rb Bose-Einstein condensation, J. Opt. Soc. Am. B **38**, 3269 (2021).

[41] J. H. Kim, D. Hong, and Y. Shin, Observation of two sound modes in a binary superfluid gas, Phys. Rev. A **101**, 061601(R) (2020).

[42] J. H. Kim, D. Hong, K. Lee, and Y. Shin, Critical en ergy dissipation in a binary superfluid gas by a moving magnetic obstacle, Phys. Rev. Lett. **127**, 095302 (2021).

[43] Z. Meng, L. Wang, W. Han, F. Liu, K. Wen, C. Gao, P. Wang, C. Chin, and J. Zhang, Atomic Bose-Einstein condensate in twisted-bilayer optical lattices, Nature (London) **615**, 231 (2023).

[44] X. Zeng, G. Ungar, Y. Liu, V. Percec, A. E. Dulcey, and J. K. Hobbs, Supramolecular dendritic liquid quasicrystals, Nature (London) **428**, 157 (2004).

[45] K. Hayashida, T. Dotera, A. Takano, and Y. Matsushita, Polymeric quasicrystal: Mesoscopic quasicrystalline tiling in *ABC* star polymers, Phys. Rev. Lett. **98**, 195502 (2007).

[46] S. Fischer, A. Exner, K. Zielske, J. Perlich, S. Deloudi, W. Steurer, P. Lindner, and S. Förster, Colloidal quasicrystals with 12-fold and 18-fold diffraction symmetry, Proc. Natl. Acad. Sci. USA **108**, 1810 (2011).

[47] C. Xiao, N. Fujita, K. Miyasaka, Y. Sakamoto, and O. Terasaki, Dodecagonal tiling in mesoporous silica, Nature (London) **487**, 349 (2012).

[48] J. Zhang and F. S. Bates, Dodecagonal quasicrystalline mor phology in a poly(styrene-*b*-isoprene-*b*-styrene-*b*-ethylene

oxide) tetrablock terpolymer, J. Am. Chem. Soc. **134**, 7636 (2012).

[49] A. J. Archer, A. M. Rucklidge, and E. Knobloch, Quasicrystalline order and a crystal-liquid state in a soft-core fluid, Phys. Rev. Lett. **111**, 165501 (2013).

[50] A. Scacchi, W. R. C. Somerville, D. M. A. Buzza, and A. J. Archer, Quasicrystal formation in binary soft matter mixtures, Phys. Rev. Res. **2**, 032043(R) (2020).

[51] D. S. Petrov, M. Holzmann, and G. V. Shlyapnikov, Bose-Einstein condensation in quasi-2D trapped gases, Phys. Rev. Lett. **84**, 2551 (2000).

[52] W. H. Press, S. A. Teukolsky, W. T. Vetterling, and B. P. Flannery, *Numerical Recipes*, 3rd ed. (Cambridge University Press, Cambridge, UK, 2007).

[53] A. Mendoza-Coto, M. Bonifacio, and F. Piazza, Low-energy excitations in bosonic quantum quasicrystals, Phys. Rev. Lett. **134**, 136003 (2025).